RESEARCH ARTICLE

RESPIRATORY COMPLEXES

Structural basis of mammalian respiratory complex I inhibition by medicinal biguanides

Hannah R. Bridges[1]*, James N. Blaza[1,2], Zhan Yin[1], Injae Chung[1], Michael N. Pollak[3], Judy Hirst[1]*

The molecular mode of action of biguanides, including the drug metformin, which is widely used in the treatment of diabetes, is incompletely characterized. Here, we define the inhibitory drug-target interaction(s) of a model biguanide with mammalian respiratory complex I by combining cryo–electron microscopy and enzyme kinetics. We interpret these data to explain the selectivity of biguanide binding to different enzyme states. The primary inhibitory site is in an amphipathic region of the quinone-binding channel, and an additional binding site is in a pocket on the intermembrane-space side of the enzyme. An independent local chaotropic interaction, not previously described for any drug, displaces a portion of a key helix in the membrane domain. Our data provide a structural basis for biguanide action and enable the rational design of medicinal biguanides.

The biguanide metformin is central to the treatment of millions of patients with type 2 diabetes worldwide (*1*) and has been studied intensely in recent years for treatment of other conditions, including ischemia-reperfusion injury (*2*, *3*), fibrosis (*4*), viral infections (*5*), and cancer (*6*). Optimization of biguanides for distinctive indications has been hindered by incomplete understanding of their molecular pharmacology, and although preclinical evidence for the antineoplastic action of metformin was sufficient to justify dozens of clinical trials (*7*), the results have been disappointing (*8*, *9*). Biguanides have been reported to target many cellular proteins, including mitochondrial glycerophosphate dehydrogenase (mGPD) (*10*), presenilin enhancer 2 (*11*), F_1F_O adenosine 5′-triphosphate (ATP) synthase (*12*), cytochrome *c* oxidase (*13*), and the chloride intracellular channel 1 (*14*). Several studies have described biguanide inhibition of mitochondrial respiratory complex I (proton-translocating NADH:ubiquinone oxidoreductase, where NADH is the reduced form of NAD^+) (*12*, *15*–*18*), supporting a mode of biguanide action in which decreased production of ATP from oxidative phosphorylation triggers the activation of adenosine 5′-monophosphate kinase and inhibition of adenylate cyclase, leading to beneficial downstream effects on gluconeogenic enzymes (in diabetes) and mTOR (in cancer and antiviral treatments) (*1*, *6*, *18*, *19*).

Complex I is a 1-MDa multiprotein assembly that is central to mitochondrial and cellular metabolism. It oxidizes the NADH produced by oxidation of carbohydrates and lipids to maintain the redox state of the mitochondrial nicotinamide adenine dinucleotide (NAD^+) pool, reduces ubiquinone-10 to drive the respiratory chain and oxygen consumption, and pumps protons out of the mitochondrial matrix. This proton pumping contributes to the proton-motive force (PMF) that drives ATP synthesis through oxidative phosphorylation (*20*). Cryo–electron microscopy (cryo-EM) studies of complex I have revolutionized our understanding of its structure, mechanism, and regulation, informing on redox catalysis in the hydrophilic domain, proton translocation across the membrane, and possible mechanisms of coupling between ubiquinone-10 reduction and proton translocation (*21*, *22*). Furthermore, cryo-EM has discriminated different resting states of the enzyme (*22*–*25*) on the basis of domain-level reorientations linked to altered conformational states of the quinone-binding channel (Q-channel): the "active" state with a structurally ordered, turnover-ready Q-channel and the pronounced "deactive" state with a locally disordered Q-channel that requires restructuring and reactivation for catalysis. Biguanides bind with an unusual preference to the deactive state of the enzyme (*16*), but their binding site(s) and modes of interaction are unknown: They are expected to bind in a site downstream of the Fe-S clusters (*12*) but do not inhibit in a simple competitive manner. Their interaction site is expected to be amphipathic on the basis of the biguanide positive charge and strong correlations between inhibitory potency, cytotoxicity, and hydrophobicity (*12*, *26*).

We use cryo-EM to reveal the molecular interactions of biguanides with mammalian respiratory complex I, defining how they inhibit catalysis. We identify distinctive binding modes and rationalize biguanide protein-state selectivity to enable future implementation of structure-based drug design in the development of biguanide-based therapies for diverse applications.

[1]MRC Mitochondrial Biology Unit, University of Cambridge, The Keith Peters Building, Cambridge Biomedical Campus, Cambridge CB2 0XY, UK. [2]Structural Biology Laboratory and York Biomedical Research Institute, Department of Chemistry, The University of York, York YO10 5DD, UK. [3]Lady Davis Institute of the Jewish General Hospital and Department of Oncology, McGill University, Montreal, QC H3T 1E2, Canada.
*Corresponding author. Email: hrb@mrc-mbu.cam.ac.uk (H.R.B.); jh@mrc-mbu.cam.ac.uk (J.H.)

IM1761092 as a model biguanide for structural studies

The antidiabetic biguanides metformin and phenformin are relatively weak inhibitors of complex I, with simple molecular shapes. We sought to avoid technical risks in cryo-EM (excessive adventitious binding and reduced image contrast) from using these compounds in high millimolar concentrations by identifying a stronger-binding derivative, which would also exhibit a more distinctive cryo-EM density. For structural investigation of the complex I binding site(s) of biguanides, we therefore assessed IM1761092 (hereafter IM1092) (*27*), a more hydrophobic (log*P* 2.37) derivative of the metformin-related antidiabetic biguanide phenformin (log*P* 0.34) that contains a 3-chloro-4-iodo-phenyl ring (Fig. 1A and fig. S1). IM1092 inhibits cellular oxygen consumption (fig. S1D) and exhibits a stronger inhibition of complex I catalysis in bovine heart mitochondrial membranes than phenformin and metformin [half-maximal inhibitory concentration (IC_{50}) in the membrane is more than 10 and 2000 times lower, respectively, depending on the conditions; Fig. 1, B and C]. Its behavior is thus consistent with the reported correlation between biguanide inhibitory potency (IC_{50}) and hydrophobicity (log*P*) (*28*).

Mammalian mitochondrial membranes "as-prepared" contain a mixture of active and deactive complex I. In the deactive state, an important structural feature of the Q-channel, the loop between TMH1 and -2 in subunit ND3 (ND3 TMH1-2 loop) that carries Cys^{39} is disordered (*24*, *25*), but in the active state, it is ordered and Cys^{39} is buried (*23*, *25*, *29*, *30*). The two states can be discriminated biochemically by their sensitivity to *N*-ethyl maleimide (NEM), which derivatizes ND3-Cys^{39} in the deactive state, preventing catalysis, but leaves the active state unaffected. We found biguanide inhibition depends on the amount of the deactive state present in membranes (Fig. 1B). As-prepared membranes incubated with both 200 μM IM1092 (10 × IC_{50}) and NEM at 4°C exhibited essentially the same deactive content as biguanide-free controls (fig. S2A), indicating that biguanides do not shift the deactive:active population equilibrium in this condition. Furthermore, biguanide inhibition is stronger at higher pH (Fig. 1C). As biguanides [pK_a ~11 (where K_a is the acid dissociation constant) (*31*)] remain singly protonated at all pH levels tested, the pH dependence likely arises from changes in the protein, such as in local charges on residue side chains or phospholipid headgroups, or conformational changes. Having established that IM1092 inhibits cellular

oxygen consumption and shares the same selectivity for inhibiting catalysis by binding to the deactive state of complex I that is observed for antidiabetic biguanides, as well as the same pH-dependent mode of action, we proceeded with this tighter-binding synthetic biguanide as a representative model compound for structural studies for the technical reasons outlined previously.

To investigate the selectivity of biguanides for different states, IM1092 was added to the mixed population of states in the purified resting enzyme, without purposeful deactivation, for cryo-EM. No substrates were added because inhibition is weaker when biguanides are added during catalysis, rather than before (*12*). IM1092 has an IC_{50} value of 86 μM for catalysis of detergent-solubilized, purified bovine complex I (fig. S2B), and cryo-EM grid conditions with 350 μM IM1092 were chosen to maximize binding within the limits of pH- and biguanide-induced protein aggregation at high concentrations (fig. S2). When purified complex I (fig. S3) was incubated in the same conditions as for cryo-EM grid preparation and then diluted into inhibitor-free assay buffer, 98% of the control catalytic rate was recovered (fig. S2F), demonstrating full reversibility of inhibition under this condition.

Overview of cryo-EM particle populations

A total of 17,203 micrographs collected from a single cryo-EM grid yielded 598,287 good particles, which refined to an estimated global resolution of 2.1 Å (fig. S4), but with such a high degree of heterogeneity that it was not possible to model parts of the map. Subsequent global classification yielded three major classes resembling the active and deactive states mentioned

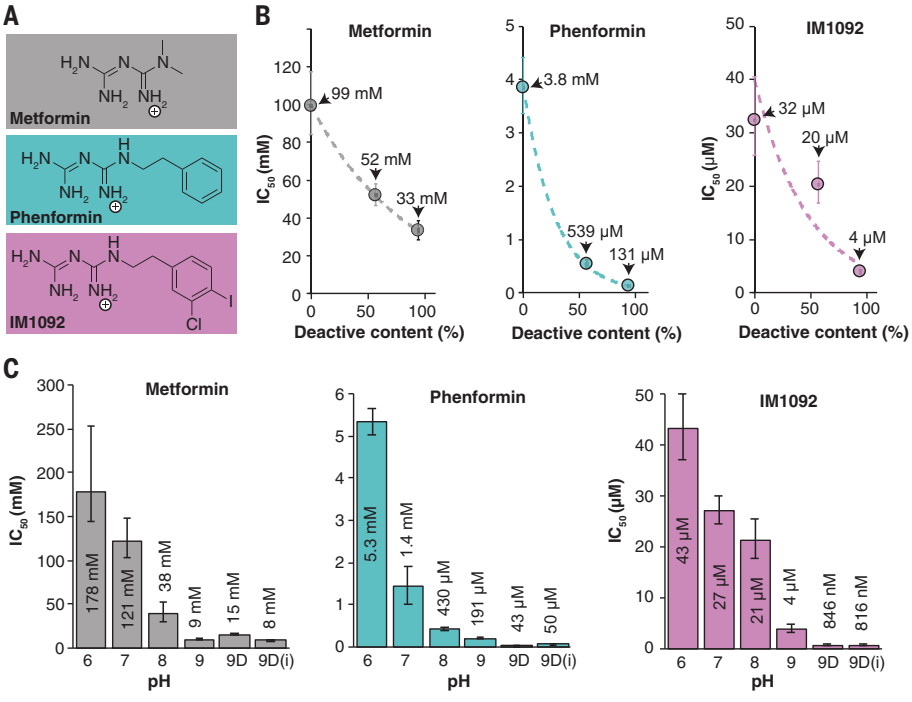

Fig. 1. Characterization of biguanide effects on catalysis and regions of structural interest. (**A**) Chemical structures of metformin, phenformin, and IM1092 in monoprotonated form. (**B**) Correlation between membrane deactive complex I content and IC_{50} for metformin (gray), phenformin (teal), and IM1092 (orchid). Error bars represent SEM for deactive content and 95% confidence intervals for IC_{50}. Data are fit to an exponential regression for visualization. (**C**) Effect of pH on IC_{50} in bovine heart membranes for metformin (gray), phenformin (teal), and IM1092 (orchid). 9D, pH 9 deactivated membranes; 9D(i), pH 9 deactivated membranes measured in the presence of antimycin A to inhibit complex III and the alternative oxidase to oxidize quinol by a different route, confirming inhibition is on complex I. Error bars represent 95% confidence intervals.

Table 1. Key characteristics of classes presented in this work. Unclear, unclear binding position, but confident identity; unidentified, the presence of density of unknown nonprotein origin.

Model	Classification scheme	PDB ID	Features		
			Q-channel ($C\text{-}C_{mask}$)	ND5 and NDUFB4 interface	ND2, NDUFB5, and NDUFA11 ($C\text{-}C_{mask}$)
Active inhibitor-free	Inhibitor-free (fig. S5)	7QSD	No density	Intact	NDUFC2 N terminus
Active-1092-i	Q-channel (fig. S7)	7R41	Unidentified	Mixed	IM1092-bound (0.49)
Active-1092-ii	Lateral helix (fig. S8)	7R42	Unidentified	Intact	IM1092-bound (0.52)
Active-1092-iii	Lateral helix (fig. S8)	7R43	Unidentified	Displaced	Unidentified
Active-1092-iv	Lateral helix (fig. S8)	7R44	Unidentified	Disordered	IM1092-bound (0.63)
Deactive-1092-i	Q-channel (fig. S7)	7R45	IM1092-bound (0.66)	Mixed	IM1092-bound (0.60)
Deactive-1092-ii	Q-channel (fig. S7)	7R46	IM1092-bound (0.72)	Mixed	Unidentified
Deactive-1092-iii	Q-channel (fig. S7)	7R47	IM1092-bound (0.68)	Mixed	IM1092-bound (0.68)
Deactive-1092-iv	Lateral helix (fig. S8)	7R48	IM1092-bound (0.66)	Intact	IM1092-bound (0.65)
Deactive-1092-v	Lateral helix (fig. S8)	7R4C	IM1092-bound (0.71)	Displaced	IM1092-bound (0.64)
Deactive-1092-vi	Lateral helix (fig. S8)	7R4D	IM1092 unclear	Disordered	IM1092-bound (0.67)
Slack-1092-i	Q-channel (fig. S7)	7R4F	IM1092 unclear	Mixed	IM1092-bound (0.65)
Slack-1092-ii	Q-channel (fig. S7)	7R4G	IM1092-bound (0.64)	Mixed	IM1092-bound (0.64)

above and a state called slack (supplementary text), which is of unknown functional relevance but has been described previously in cryo-EM studies of bovine complex I (*22*, *24*, *25*). Inhibitor-free reference maps of bovine complex I from separate inhibitor-free preparations in detergent [figs. S5 and S6 and EMD-3731 (*24*)] were used for comparison to identify and evaluate features found in the maps with IM1092 present. Three regions of interest are (i) densities occupying the Q-channel; (ii) unusually poor density in a portion of the C-terminal lateral helix in subunit ND5 and the adjacent subunit NDUFB4; and (iii) altered density at the expected position of the NDUFC2 subunit N terminus. Different classification strategies were tested to disentangle the different states and IM1092 interactions, leading to implementation of a "local-first" classification regime (supplementary text) used in two separate schemes to describe 12 distinct classes (Table 1 and figs. S7 to S9).

Biguanide-binding site 1: Ubiquinone-binding channel

Density was observed in the Q-channel, close to its entrance from the membrane, in all three major classes. Using local-first classification (fig. S7), we separated the particles into one active class (Active-1092-i; fig. S10), three deactive classes (Deactive-1092-i, -ii, and -iii; figs. S11 to S13), and two slack classes (Slack-1092-i and -ii; Table 1 and figs. S14 and S15). The major classes were assigned by global comparisons to reference maps and key local features (table S1 and supplementary text). Densities for IM1092 in the Q-channel are clear in the Deactive-1092-i, -ii, and -iii and Slack-1092-ii maps (Fig. 2, C to E and H, and figs. S16 and S17), and the cross-correlation fits (C-C_{mask}) (*32*) for the fit of the IM1092 molecule into its density were high (0.66 to 0.72) (Table 1). In Slack-1092-i, although the density is consistent for the chloro-iodo-phenyl moiety, the biguanide moiety of the putative IM1092 molecule was insufficiently resolved to confidently model its orientation (Fig. 2G). The density in the Active-1092-i map occupies a position similar to that of the densities observed in the other classes (Fig. 2F), but a smaller additional density feature is also observed further into the Q-channel so that, together, they resemble density observed in the Q-channel of the active-apo (inhibitor-free) class of bovine complex I in nanodiscs (EMD-14133) (*22*). With an IM1092 molecule refined in different orientations into the density in the Active-1092-i map near the Q-channel entrance, C-C_{mask} values are low (<0.5), and the shape of the density was visibly a poor fit; the second density was too small and featureless to ascertain its origin, and the identity of these two densities remain unconfirmed. Overall, ~45 to ~60% of the total population and ~56 to ~75% of the (deactive and slack) population presents clear evidence of IM1092 occupying the Q-channel.

In the deactive and slack states, IM1092 binds in an amphipathic site straddling two zones of the Q-channel: the hydrophobic region next to the exit (Fig. 2A) and the charged central region of the channel (*33*). The chloro-iodo-phenyl group of IM1092 points toward the channel exit (Fig. 2A), forming weak halogen bonds from the Cl to the ND1-Pro^{48} carbonyl and from the I to the S of ND1-Met^{225}, as well as van der Waals interactions with ND1-Phe^{224}, ND1-Phe^{220}, ND1-Leu^{55}, and NDUFS7-Trp^{46}. The halogen bonds are specific to IM1092, relative to phenformin, likely contributing to its higher binding affinity; and metformin, which lacks the phenyl ring, is not stabilized by the above interactions or by π-stacking to ND1-Phe^{224}, consistent with its much lower binding affinity. The biguanide moiety faces into the channel, toward the charged region, and adopts a range of different orientations (Fig. 2, C to E and H). In the Deactive-1092-i and Slack-1092-ii states, it forms a cation-π interaction with NDUFS7-Trp^{46} and, in the Deactive-1092-i state, a weak ionic interaction with the ND1-Glu^{24} carboxyl also. In the Deactive-1092-ii and -iii states, its orientation brings it closer

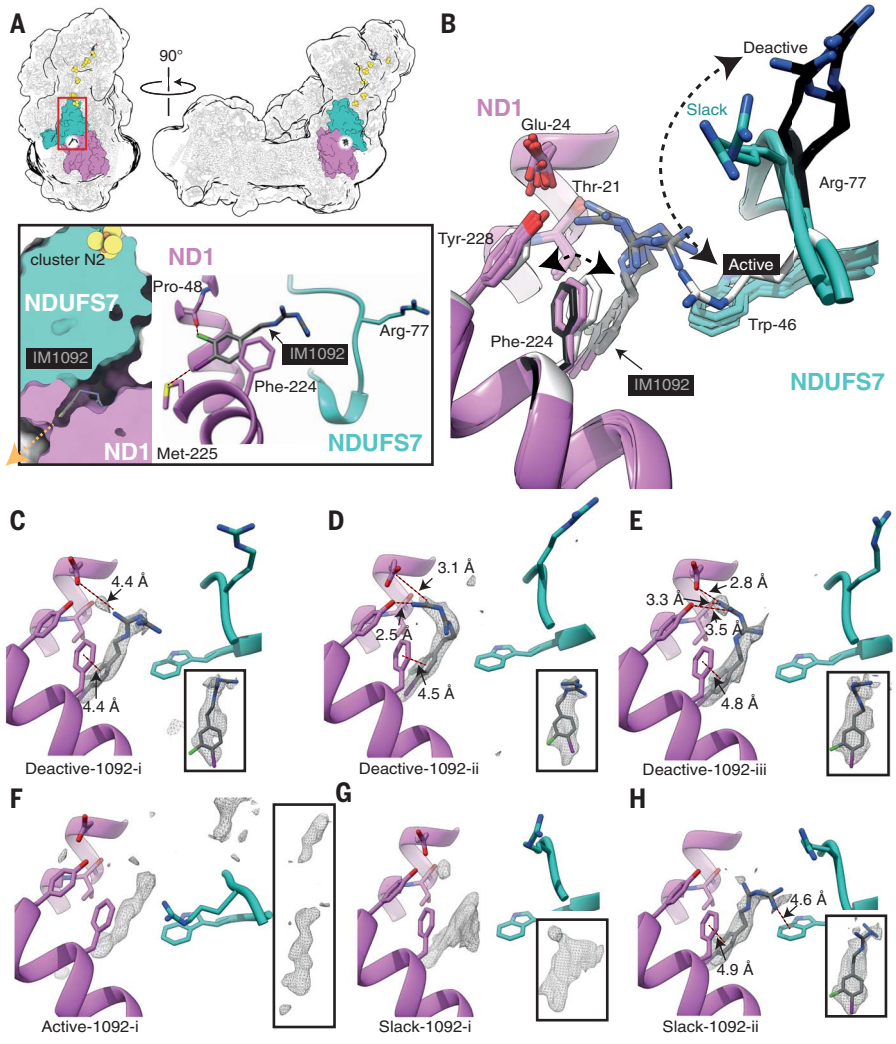

Fig. 2. Binding of IM1092 in the Q-channel. (**A**) Overview showing the location of the biguanide-binding site and inset showing a closer view and bonding interactions of the chloro-iodo-phenyl group for Deactive-1092-i. Orange arrow shows the route for exit from the Q-channel into the lipid bilayer. (**B**) Overlay of models for the Active-1092-i; Deactive-1092-i, -ii, and -iii; and Slack-1092-i and -ii states, aligned to subunit ND1, showing the location and variability of biguanide-binding orientations and relative position of NDUFS7-Arg^{77}. NDUFS7-Arg^{77} and ND1-Phe^{224} are white in the active models, mint or orchid in the slack models, and black in the deactive models. (**C** to **H**) Cryo-EM difference map densities (composite versus models) for biguanides bound to Deactive-1092-I (C), Deactive-1092-ii (D), Deactive-1092-iii (E), Active-1092-i (F), Slack-1092-i (G), and Slack-1092-ii (H). The insets show the difference map density for the biguanide for each model shown. Biguanides are not modeled in (F) and (G), owing to uncertainties in the ligand identity or orientation. Side-chain and ligand density for (C) to (H) are shown in fig. S16.

to ND1-Glu[24], and it forms a hydrogen bond with the ND1-Tyr[228] hydroxyl. In each state with modeled biguanide, the experimental IM1092 map density at higher thresholds is consistent with a mixture of inhibitor binding poses.

Notably, the conformation of the biguanide-binding region of the Q-channel differs between the three major states (*21*–*23*), regardless of whether an inhibitor is bound (Fig. 2B). Notably, NDUFS7-Arg[77] swings in an arc from its position in the active state, with its side chain pointing toward the Q-channel exit, to point approximately toward cluster N2 in the deactive state, adopting an intermediate position in the slack state (Fig. 2B). The NDUFS7-Arg[77] guanidinium is ~7 Å (slack) and 10 to 14 Å (deactive) away from the bound biguanide (N-N distance), but only ~4 Å away when IM1092 is refined into the density in the Active-1092-i map in the same orientation, indicating that repulsion between their positive charges may disfavor biguanide binding in the active state.

Available Protein Data Bank (PDB) models for mammalian, fungal, bacterial, and plant complexes I were compared to assess the conservation of key residues interacting with the biguanide moiety; NDUFS7-Trp[46], ND1-Glu[24], ND1-Tyr[228], and NDUFS7-Arg[77] are conserved in all species surveyed. The only high-quality reported human mutation in these residues in the ClinVar database (*34*) is the ND1-E24K (Glu[24]→Lys) mutation associated with Leber hereditary optic neuropathy–mitochondrial encephalopathy, lactic acidosis, and stroke-like episodes (LHON-MELAS) overlap syndrome (*35*). Human mutations of the residues involved in the biguanide-binding site are therefore rare, consistent with their important role in enzyme function. Because they are mitochondrially encoded and/or essential for function, these residues cannot easily be artificially mutated in a mammalian system. Methods for mutating mitochondrial DNA are advancing, but site specificity and the efficiency of reaching homoplasmic edits remain challenging (*36*).

Biguanide interaction site 2: ND5 lateral helix and NDUFB4 interface

Transmembrane subunit ND5 contains an unusual long helix that runs laterally alongside ND4 and ND2, which has been proposed to either stabilize the proton-pumping modules or act as a transmissive element in proton pumping (*37*). Substantial evidence of disorder at the ND5 lateral helix–subunit NDUFB4 interface was observed in preliminary maps, so the dataset was subject to a separate local-first classification that focused on this region (figs. S8 and S18). The strategy yielded three major classes: one with a typical well-ordered ND5 lateral helix and NDUFB4 and two with distortion or disordering of ND5 residues 547 to 564 and nearby NDUFB4 residues 77 to 92. The classes were further separated into Active-1092-ii, -iii, and -iv (figs. S19 to S21); Deactive-1092-iv, -v, and -vi (Table 1 and figs. S22 to S24); and three slack classes, which all displayed poor density for the downstream ND5 lateral helix and were not further investigated. Overall, ~65% of the protein population was perturbed in this region, with similar proportions observed for active, deactive, and slack (~52, ~66, and ~58%, respectively). Deactive classes with a disrupted helix exhibit a small "opening" of the angles between the membrane and hydrophilic domains and distal and proximal membrane domains compared with their better-ordered equivalents (fig. S25 and supplementary text).

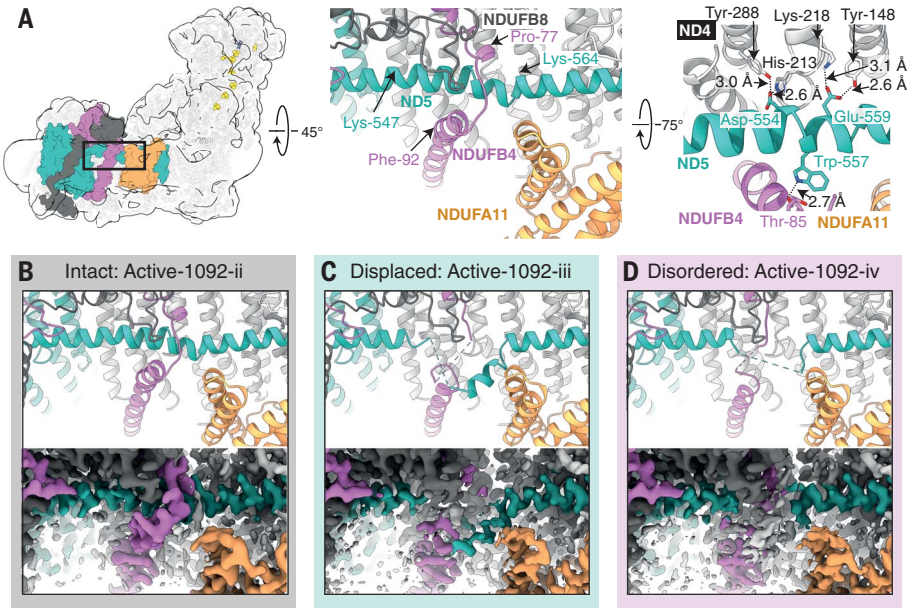

Fig. 3. Biguanide-induced distortion and disordering of the ND5 lateral helix and NDUFB4 loop. (**A**) Location of the structure disturbance and two views of the model of Deactive-1092-iv with hydrogen-bonding interactions indicated with black dotted lines and distances indicated. Orchid, NDUFB4; teal, ND5; orange, NDUFA11; dark gray, NDUFB8. Side-chain density for this region of Deactive-1092-iv is shown in fig. S18. (**B** to **D**) Models and composite cryo-EM maps for Active-1092-ii (B), Active-1092-iii (C), and Active-1092-iv (D) showing progressive disordering within the series. Details of π-bulge stabilizing interactions and equivalent disordering for the deactive states (Deactive-1092-iv, -v, and -vi) are shown in fig. S18.

This interesting region of the usually well-ordered ND5 lateral helix does not form a perfect α helix even in inhibitor-free active or deactive mammalian enzyme structures (*21*–*25*). The Active-1092-ii and Deactive-1092-iv models match the well-ordered inhibitor-free active model in this region. Two π-bulges (fig. S18) are stabilized by interactions between the lateral helix and nearby waters and by ionic and hydrogen bonding to ND4 (Fig. 3A, right).

In Active-1092-iii and Deactive-1092-v (referred to as displaced), a short portion of the ND5 lateral helix is altered: Lys[547] to Ser[550] are disordered, and an interruption of the helical structure at Leu[562] to Pro[563] allows a short stretch of helix (residues 550 to 559) to move outwards, away from the complex, and laterally, along the membrane plane (Fig. 3 and fig. S18). A loop in NDUFB4 at residues 78 to 83, which usually wraps around the lateral helix, becomes disordered from Pro[77] to Leu[91]. In Active-1092-iv and Deactive-1092-vi (referred to as disordered), the whole ND5 region from Lys[547] to Lys[564] appears disordered, along with the NDUFB4 loop described previously (Fig. 3D and fig. S18). Although not observed in the detergent-solubilized protein, the bovine enzyme in nanodiscs (*22*) contains two phospholipids near to the distorted region. No nearby density features can be interpreted as a tightly bound biguanide. Considering the positive charge on IM1092, it may interact with ND5-Asp[554] and/or Glu[559], thereby disrupting hydrogen bonding from the lateral helix to subunit ND4, or interact with nearby stabilizing phospholipids. Generally, π-bulges are energetically unfavorable elements (*38*) that require stabilization by hydrogen bonding to polar side chains or water molecules (*39*). The strained nature of this region may make it particularly prone to destabilization by guanidium-like biguanides. No mutations of Asp[554] or Glu[559] are observed in the ClinVar database (*34*), and acidic residues in these positions are conserved in current mammalian and plant structures, which suggests their important role in stabilizing the membrane domain.

Biguanide-binding site 3: ND2, NDUFB5, and NDUFA11

Density that matches IM1092 was observed in a pocket formed by subunits ND2, NDUFB5, and NDUFA11 on the intermembrane-space

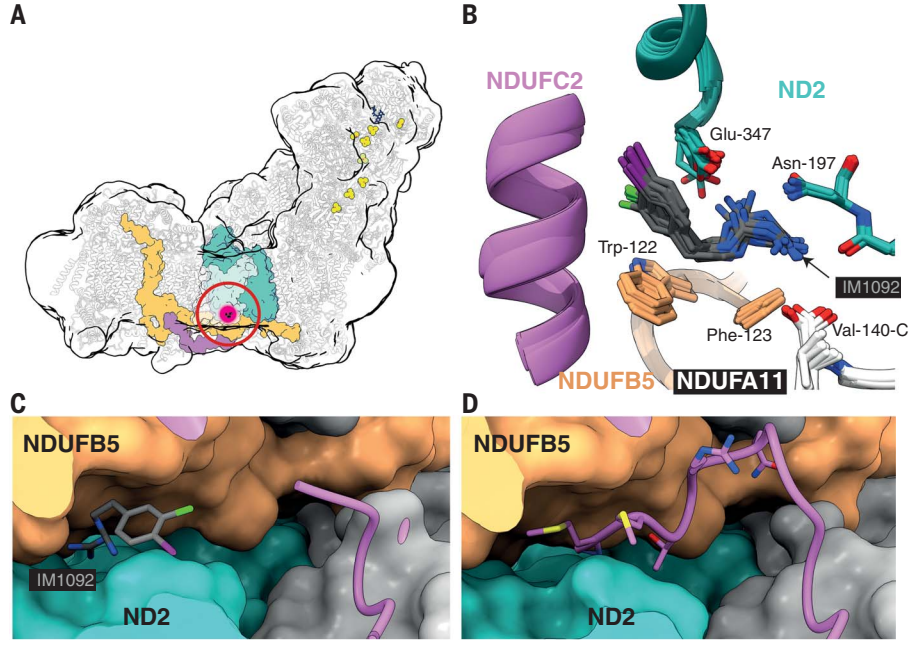

Fig. 4. Location of the biguanide binding at the ND2-NDUFB5-NDUFA11 interface. (**A**) Overall location of the binding site. Purple, NDUFC2; teal, ND2; orange, NDUFB5. (**B**) Overlay of all models aligned to ND2. White, NDUFA11; Val-140-C, C terminus of NDUFA11. (**C**) Surface representation (Active-1092-ii model) showing subunit NDUFC2 in cartoon, with atoms shown for IM1092. (**D**) Same view from the active inhibitor-free model showing the atoms from residues 1 to 7 of NDUFC2. Local interactions and density for the individual maps and models are shown in figs. S26 and S27.

side of the enzyme (Fig. 4 and figs. S26 and S27). The pocket is occupied by the N-terminal seven residues of NDUFC2 in the inhibitor-free enzyme, both in n-dodecyl-B-D-maltoside (DDM) and in all states of the bovine enzyme in nanodiscs (*22*). The NDUFC2 N terminus is displaced by the biguanide, with inhibitor densities observed in most classes in this study (figs. S26 and S27). The biguanide moiety is stabilized by an ionic interaction with ND2-Glu^{347} and by hydrogen bonds with the ND2-Tyr^{196} backbone carbonyl, ND2-Thr^{199} hydroxyl, ND2-Asn^{197} side chain, and NDUFA11-Val^{140} C-terminal carboxyl, as well as nearby water molecules resolved in some maps (figs. S26 and S27). The IM1092 bound in this site does not interfere with any known catalytically relevant structural elements in the complex and so is likely to represent a noninhibitory interaction.

Independence of interaction sites

The two local classification schemes used (figs. S7 and S8) each yielded six models, and a summary of their key features is shown in Table 1. All six classes from Q-channel classification (fig. S7) had poor density for the ND5-NDUFB4 interface, consistent with a mixture of the three lateral helix states being represented there. Overall, ~65% of the imaged protein population is disrupted in this region (fig. S8), and disorder is observed in all three major classes, as well as in states with (e.g., Deactive-1092-i) or without clear binding of IM1092 at the Q-channel (Active-1092-i). Furthermore, in the classes from the lateral helix classification (fig. S8), density for IM1092 was observed in the Q-channel of deactive classes with both ordered and displaced lateral helix. Taken together, biguanide binding in the Q-channel and the state of the lateral helix are not correlated. IM1092 is observed in the ND2, NDUFB5, and NDUFA11 pocket regardless of the occupancy of the Q-channel or the status of the lateral helix (Table 1). Therefore, the three interaction sites are independent of one other.

Discussion

Biguanide access to complex I binding sites

Substantial inhibition of complex I in vivo requires the biguanide positive charge, an inherent feature of the two cojoined guanidinium moieties at physiological pH (*31*), to drive biguanide accumulation in the mitochondrial matrix (*40*) by up to 1000-fold relative to the cytosol in response to the mitochondrial PMF. This mitochondrial concentrating effect makes the intramitochondrial biguanide concentration sufficient for the inhibition of targets with only relatively weak biguanide affinity, such as complex I, making them as potentially relevant as targets outside of the mitochondrial matrix that exhibit greater intrinsic affinities, such as rat mGPD (*10*). Recent work has questioned mGPD itself as a therapeutic target because metformin was found to be noninhibitory against the human enzyme (*41*). All three interaction or binding sites described in complex I contain acidic residues close to the membrane-aqueous interface, suggesting that IM1092 accesses them from the membrane, likely with the chloro-iodo-phenyl group acting as an anchor into the hydrophobic membrane core and the hydrophilic biguanide moiety interacting with the negatively charged phosphate headgroups, as proposed previously (*42*, *43*). The most likely route of access for hydrophobic biguanides to the Q-channel is therefore via the matrix-facing phospholipid leaflet. Although the Q-channel is reproducibly well ordered in the active state, deactive (or slack) states have mobile regions of the Q-channel loops that face the mitochondrial matrix (*21*–*24*, *44*), so it is also possible that the Q-channel may become exposed to the matrix in these states, providing an alternative route for hydrophilic biguanides with poor membrane solubility, such as metformin, to enter the Q-channel.

Major inhibitory site and selectivity for the deactive state

Biguanides, including IM1092 and the antidiabetic compounds metformin and phenformin, all share a preference to bind to the deactive state of complex I. This behavior is not observed for any other class of complex I inhibitor, and we expect all three biguanides to share the same inhibitory binding site and mode of action. In comparison with canonical hydrophobic complex I inhibitors such as rotenone, biguanides are relatively hydrophilic, water-soluble molecules that are unlikely to bind in highly hydrophobic or membrane-intrinsic sites. We suggested previously that metformin might interact at the junction of the hydrophilic and hydrophobic domains where a set of mobile elements (in subunits NDUFS7, NDUFS2, ND3, and ND1) change their conformation between the active and deactive states by binding to a resting state and preventing a return to catalysis (*12*). Our structures now demonstrate that the biguanide-binding site is inside the Q-channel, in a region that likely becomes exposed to the matrix in the deactive state, and adjacent to the mobile element in NDUFS7 that carries Arg^{77} and that switches its conformation between the active and deactive states.

In the Q-channel, IM1092 binds in an amphipathic region with the biguanide moiety stabilized by hydrogen bonding, cation-π interactions, and ionic bonding, and the hydrophobic chloro-iodo-phenyl group is stabilized by weak halogen bonding and van der Waals interactions. These additional stabilizing interactions between the hydrophobic portion of the Q-binding site and hydrophobic biguanides explain the relationship observed previously between biguanide hydrophobicity and inhibitory potency (*12*). Other neutral and highly hydrophobic ligands (DDM, cholate, rotenone, and IACS-2858) have also been observed binding

in overlapping sites in various protein states (fig. S28) (*21*, *22*, *45*). Yet biguanides remain distinctive inhibitors in their state selectivity, shown here and previously (*16*). Of the other inhibitors, only rotenone has been demonstrated to bind to a deactive-like open state, but the binding was not state specific (*21*) and the protein interactions and in vivo effects of biguanides and rotenone are different (*46*, *47*).

Despite the locations of the biguanide- and ubiquinone-binding sites overlapping, metformin does not display classical competitive behavior (*12*). This is likely because neutral, hydrophobic inhibitors such as piericidin A, IACS-2858, and acetogenin (*45*, *48*, *49*) compete for (active-like) enzyme states capable of forming the Michaelis complex, but biguanide binding occurs most readily in deactive-like states that are not preorganized, owing to disordering of the Q-channel loops in NDUFS2, ND3, and ND1 (*24*). The deactive state of complex I is stabilized by high pH (*50*), and we see a strong correlation between pH and inhibitory potency. Weak biguanide inhibition of active complex I could originate either from binding to the Q-channel or from an inhibitory nature to the ND5 lateral helix interaction. The conformation of the NDUFS7 β1–β2 loop that contains Arg^{77} differs between the active, deactive, and slack states. Biguanides bind 7 to 14 Å from Arg^{77} in deactive and slack states, but the arginine guanidinium position is shifted relative to the positions in the DDM- and cholate-bound bovine nanodisc deactive and slack states (PDB IDs 7QSM and 7QSO) (fig. S28) (*22*). In all active models, Arg^{77} is much closer to the putative biguanide-binding site (Fig. 2B), presenting a source of steric hindrance and charge repulsion that acts against strong inhibitory binding and explains the preference of biguanide inhibitors to bind to NEM-sensitive (deactive) complex I [manifesting as a lower IC_{50} for deactivated complex I (Fig. 1B) (*16*)]. Biguanides are less powerful inhibitors when added during catalysis rather than before (*12*), and metformin has been proposed to act by slowing down activation (*51*) rather than by classical inhibition. Our data support an inhibitory mode that primarily acts by preventing reactivation of the resting deactive state, and we conclude that the major inhibitory interaction site of biguanides is the Q-channel.

Local chaotropic drug-protein interactions

A key feature of biguanide interactions with complex I is the displacement and disordering of a portion of the ND5 lateral helix. This type of localized disruption has not been observed previously but may be facilitated by nonspecific interactions with phospholipids (*42*). Considering the similarity of biguanides to the well-known chaotrope and protein denaturant guanidinium, the biguanide may be attracted to the negatively charged ND5-Asp^{554} and ND5-Glu^{559} and specifically destabilize the hydrogen-bonding networks between the lateral helix and subunit ND4. In particular, biguanide binding could weaken the interactions of the lateral helix π-bulge segment, allowing secondary structure shifts to form an α helix and a disordered loop. After this process, the unraveled segment of the helix would no longer provide lateral support to keep the strained junction between ND2 and ND4 (*52*) tightly together, explaining the slight "opening" of the proximal and distal membrane domain interface (fig. S25). Protein stability assays (fig. S2) suggest that complex I is stabilized close to the IM1092 IC_{50} ranges but is destabilized at higher concentrations, and we interpret this behavior to indicate that binding to the Q-channel (and/or ND2-NDUFB5 interface) stabilizes the protein and that chaotropic action occurs at higher concentrations. Our structures in this study are in a detergent micelle with tightly bound lipids present, and the chaotropic interaction site we observe is within the phospholipid headgroup plane. Notably, any inhibitory consequences of structural disturbance in this study are fully reversible, which is demonstrated by full recovery of activity after inhibitor dilution (fig. S2F). We propose that biguanides such as metformin, phenformin, and related drug leads could exert similar local chaotropic actions on any number of cellular proteins, especially membrane proteins, to inhibit or stimulate their usual functions, presenting a novel mode of enzyme-drug interaction and a potential explanation for the breadth of biguanide targets identified thus far.

Implications for in vivo mechanism of action

Although other complex I inhibitor classes have been proposed as possible therapeutic compounds (*53*–*56*), biguanides appear to offer a lower toxicity profile than neutral species such as rotenone, with reduced risk of Parkinsonism (*47*). The key factor may lie in self-limitation of action in the form of negative feedback at the organelle level, meaning that their mechanism of action lowers the risk of complete inhibition of the respiratory chain. The membrane potential leads to increased concentration of biguanides at the complex I site of action, but as complex I is inhibited, the membrane potential falls (*57*), creating an equilibrium that limits the concentration and therefore the degree of inhibition. Toxicity may also be influenced by the ready reversibility of biguanide inhibition seen here and previously (*12*), compared with the irreversibility of very hydrophobic, neutral compounds. In vivo, the active-like state that binds canonical inhibitors is expected to be prevalent in normal tissues (*44*), where the opportunities for biguanides to inhibit may be restricted to the weak binding observed in this study against active-like states, or to the binding of putative catalytic intermediates where NDUFS7-Arg^{77} has moved away from the inhibitory binding site. The deactive state of complex I forms during oxygen starvation (*51*), such as during ischemia (*2*) and in solid tumor microenvironments (*58*). Discrimination of biguanides for this state means that, unlike canonical inhibitors, hypoxic tissues can be selectively targeted with less risk of also compromising mitochondrial respiration in tissues with normally functioning (active) complex I. In such low-oxygen environments, only complex I in the active state may work in the reverse direction, using the PMF and ubiquinol to drive NAD^+ reduction and reactive oxygen species production (*51*). By targeting the deactive state formed in these environments, preventing reactivation, biguanides may diminish reactive oxygen species production by reverse electron transfer, as has been observed previously for metformin (*59*).

Metformin has proven to be a safe and effective biguanide for diabetes treatment, and our data now provide a structure-based rationale for its mode of action on complex I. This work also offers a basis for future structure-based biguanide drug design for the state-specific inhibition of complex I for other potential therapeutic applications (such as cancer treatment) in which metformin has been less successful, as well as improved prediction of additional protein target binding sites for biguanide drugs.

REFERENCES AND NOTES

1. M. Foretz, B. Guigas, L. Bertrand, M. Pollak, B. Viollet, *Cell Metab.* **20**, 953–966 (2014).
2. K. Skemiene *et al.*, *Biomolecules* **10**, 1400 (2020).
3. X. Wang *et al.*, *PLOS ONE* **12**, e0182777 (2017).
4. N. Sato *et al.*, *Respir. Res.* **17**, 107 (2016).
5. S. Lehrer, *World Acad. Sci. J.* **2**, 1 (2020).
6. H. Zhao, K. D. Swanson, B. Zheng, *Trends Cancer* **7**, 714–730 (2021).
7. M. Pollak, *Nat. Med.* **20**, 591–593 (2014).
8. S. Kordes *et al.*, *Lancet Oncol.* **16**, 839–847 (2015).
9. P. J. Goodwin *et al.*, *J. Clin. Oncol.* **31**, 1033–1033 (2013).
10. A. K. Madiraju *et al.*, *Nature* **510**, 542–546 (2014).
11. T. Ma *et al.*, *Nature* **603**, 159–165 (2022).
12. H. R. Bridges, A. J. Y. Jones, M. N. Pollak, J. Hirst, *Biochem. J.* **462**, 475–487 (2014).
13. T. E. LaMoia *et al.*, *Proc. Natl. Acad. Sci. U.S.A.* **119**, e2122287119 (2022).
14. F. Barbieri *et al.*, *Front. Oncol.* **9**, 135 (2019).
15. M. Y. El-Mir *et al.*, *J. Biol. Chem.* **275**, 223–228 (2000).
16. S. Matsuzaki, K. M. Humphries, *Biochemistry* **54**, 2011–2021 (2015).
17. M. R. Owen, E. Doran, A. P. Halestrap, *Biochem. J.* **348**, 607–614 (2000).
18. G. Rena, D. G. Hardie, E. R. Pearson, *Diabetologia* **60**, 1577–1585 (2017).
19. R. A. Miller *et al.*, *Nature* **494**, 256–260 (2013).
20. J. Hirst, *Annu. Rev. Biochem.* **82**, 551–575 (2013).
21. D. Kampjut, L. A. Sazanov, *Science* **370**, eabc4209 (2020).
22. I. Chung *et al.*, *Nat. Commun.* **13**, 2758 (2022).
23. A. A. Agip *et al.*, *Nat. Struct. Mol. Biol.* **25**, 548–556 (2018).
24. J. N. Blaza, K. R. Vinothkumar, J. Hirst, *Structure* **26**, 312–319. e3 (2018).
25. J. Zhu, K. R. Vinothkumar, J. Hirst, *Nature* **536**, 354–358 (2016).
26. T. Sakai *et al.*, *Sci. Rep.* **11**, 4852 (2021).
27. S. W. Kim *et al.*, "Guanidine Compounds and use thereof," US patent application no. 2017/0073331 A1 (16 March 2017).
28. H. R. Bridges, V. A. Sirviö, A. N. A. Agip, J. Hirst, *BMC Biol.* **14**, 65 (2016).

29. M. Babot, A. Birch, P. Labarbuta, A. Galkin, *Biochim. Biophys. Acta* **1837**, 1083–1092 (2014).
30. E. V. Gavrikova, A. D. Vinogradov, *FEBS Lett.* **455**, 36–40 (1999).
31. D. Kathuria, A. A. Bankar, P. V. Bharatam, *J. Mol. Struct.* **1152**, 61–78 (2018).
32. P. V. Afonine *et al*., *Acta Crystallogr. D Struct. Biol.* **74**, 814–840 (2018).
33. J. G. Fedor, A. J. Y. Jones, A. Di Luca, V. R. I. Kaila, J. Hirst, *Proc. Natl. Acad. Sci. U.S.A.* **114**, 12737–12742 (2017).
34. M. J. Landrum *et al*., *Nucleic Acids Res.* **46**, D1062–D1067 (2018).
35. E. L. Blakely *et al*., *Eur. J. Hum. Genet.* **13**, 623–627 (2005).
36. P. Silva-Pinheiro, M. Minczuk, *Nat. Rev. Genet.* **23**, 199–214 (2022).
37. R. G. Efremov, R. Baradaran, L. A. Sazanov, *Nature* **465**, 441–445 (2010).
38. J. Ludwiczak *et al*., *Sci. Rep.* **9**, 6888 (2019).
39. J. P. Cartailler, H. Luecke, *Structure* **12**, 133–144 (2004).
40. F. Davidoff, *J. Biol. Chem.* **246**, 4017–4027 (1971).
41. M. J. MacDonald, I. H. Ansari, M. J. Longacre, S. W. Stoker, *Diabetes* **70**, 1575–1580 (2021).
42. G. Schäfer, *Biochem. Pharmacol.* **25**, 2005–2014 (1976).
43. N. Samart, C. N. Beuning, K. J. Haller, C. D. Rithner, D. C. Crans, *Langmuir* **30**, 8697–8706 (2014).
44. Z. Yin *et al*., *Nat. Commun.* **12**, 707 (2021).
45. I. Chung *et al*., *Sci. Adv.* **7**, eabg4000 (2021).
46. M. Konopleva *et al*., Targeting Oxidative Phosphorylation with a Mitochondrial Complex I Inhibitor is limited by Mechanism-based Toxicity, 1506700/v1, Research Square [Preprint] (2022).
47. S. Heinz *et al*., *Arch. Toxicol.* **93**, 2603–2615 (2019).
48. H. R. Bridges *et al*., *Nat. Commun.* **11**, 5261 (2020).
49. D. N. Grba *et al*., *J. Biol. Chem.* **298**, 101602 (2022).
50. A. B. Kotlyar, V. D. Sled, A. D. Vinogradov, *Biochim. Biophys. Acta* **1098**, 144–150 (1992).
51. A. Galkin, S. Moncada, *Interface Focus* **7**, 20160104 (2017).
52. A. Di Luca, V. R. I. Kaila, *Biochim. Biophys. Acta Bioenerg.* **1862**, 148382 (2021).
53. N. Madhusudhan *et al*., *ACS Chem. Biol.* **15**, 158–170 (2020).
54. J. R. Molina *et al*., *Nat. Med.* **24**, 1036–1046 (2018).
55. A. Naguib *et al*., *Cell Rep.* **23**, 58–67 (2018).
56. D. A. Russell *et al*., *J. Nat. Prod.* **83**, 1829–1845 (2020).
57. Z. Drahota *et al*., *Physiol. Res.* **63**, 1–11 (2014).
58. A. Emami Nejad *et al*., *Cancer Cell Int.* **21**, 62 (2021).
59. C. Batandier *et al*., *J. Bioenerg. Biomembr.* **38**, 33–42 (2006).

ACKNOWLEDGMENTS

We thank D. Chirgadze (Cambridge), J. Radecke, and Z. Yang (eBIC) for their assistance with grid screening and data collection; Diamond for access and support of the cryo-EM facilities at the UK national electron Bio-Imaging Centre (eBIC), proposals BI22238-10 and EM17057-23, funded by the Wellcome Trust, MRC, and BBSRC; members of the Hirst laboratory, especially N. Agip, for their participation in bovine mitochondrial preparations; S. McLaughlin (LMB, Cambridge) for access to the nano-DSF; T. Terwilliger (Los Alamos, NM) for guidance with map sharpening and composite map generation; S. Ding (MBU) for recording mass spectrometry data; H. Prag (MBU) for recording liquid chromatography data; P. Gierth (Cambridge) for recording nuclear magnetic resonance data; J. Bosak (MBU) for culturing and authenticating cells; and M. Iadanza (Leeds) and P. Afanasyev (ETH, Zurich) for their scripts deposited on Github. **Funding:** This work was supported by the Medical Research Council (MC_U105663141 and MC_UU_00015/2 to J.H.) and by ImmunoMet Therapeutics Inc.

Author contributions: Conceptualization: H.R.B., M.N.P., and J.H. Methodology: H.R.B. and J.N.B. Validation: H.R.B. Formal analysis: H.R.B. Investigation: H.R.B., J.N.B., Z.Y., and I.C. Data curation: H.R.B. Writing – original draft: H.R.B. Writing – review and editing: H.R.B., J.N.B., Z.Y., I.C., M.N.P., and J.H. Visualization: H.R.B. Supervision: J.H. Project administration: H.R.B. and J.H. Funding acquisition: J.H. **Competing interests:** ImmunoMet Therapeutics Inc. are the inventors on patent US2017/007331 for the biguanide compound IM1761092 used in this study. M.N.P. is on the scientific advisory board of ImmunoMet Therapeutics and holds shares in the company. The authors declare that they have no further competing interests. **Data and materials availability:** The structure data accession codes are EMD-14251, EMD-14252, EMD-14253, EMD-15254, EMD-15355, and PDB-7R41 (Active-1092-i); EMD-4256, EMD-14257, EMD-14258, EMD-14259, EMD-14260, and PDB-7R42 (Active-1092-ii); EMD-14261, EMD-14262, EMD-14263, EMD-14264, EMD-14265, and PDB-7R43 (Active-1092-iii); EMD-14266, EMD14267, EMD-14268, EMD-14269, EMD-14270, and PDB-7R44 (Active-1092-iv); EMD-4272, EMD-14273, EMD-14274, EMD14275, EMD14276, and PDB-7R45 (Deactive-1092-i); EMD-14277, EMD-14278, EMD14279, EMD-14280, EMD-14281, and PDB-7R46 (Deactive-1092-ii); EMD-14282, EMD-14283, EMD-14284, EMD-14285, EMD-14286, and PDB-7R47 (Deactive-1092-iii); EMD-14287, EMD-14288, EMD-14289, EMD-14290, EMD-14291, and PDB-7R48 (Deactive-1092-iv); EMDB-14292, EMD-14293, EMD-14294, EMD-14295, EMD-14296, and PDB-7R4C (Deactive-1092-v); EMDB-14297, EMD-14298, EMD-14299, EMD-14300, EMD-14301, and PDB-7R4D (Deactive-1092-vi); EMDB-14302, EMD-14304, EMD-14305, EMD-14306, and PDB-7R4F (Slack-1092-i); EMD-14307, EMD-14308, EMD-14309, EMD-14310, EMD-14311, and PDB-7R4G (Slack-1092-ii); EMBD-14127, EMD-14128, EMD-14129, EMD14130, EMD-14131, and PDB-7QSD (Inhibitor-free active); and EMDB-14126 (Inhibitor-free slack). Raw micrograph images are available at EMPIAR with accession codes EMPIAR-10991 (in presence of IM1761092) and EMPIAR-10984 (inhibitor-free). Otherwise, all data needed to evaluate the conclusions in the paper are present in the paper and/or the supplementary materials. IM1092 was supplied by ImmunoMet Therapeutics Inc. by collaboration agreement. ImmunoMet Therapeutics Inc. accepts proposals to supply IM1092 and ~1000 other biguanide compounds from their biguanide library for research purposes. Such proposals should be directed to dwelsch@immunomet.com.

SUPPLEMENTARY MATERIALS

science.org/doi/10.1126/science.ade3332
Materials and Methods
Supplementary Text
Figs. S1 to S28
Tables S1 to S15
References (*60*–*78*)
MDAR Reproducibility Checklist

View/request a protocol for this paper from *Bio-protocol*.

Submitted 10 August 2022; accepted 23 December 2022
10.1126/science.ade3332